Intramolecular Amino-thiolysis Cyclisation of Graphene Oxide Modified with Sulfur Dioxide: XPS and Solid-state NMR Studies

Eduardo Humeres,[*,a] Abil E. Aliev,[*,b] Alessandra Smaniotto,[a,1]Rafael Brognoli,[a]

Nito Angelo Debacher,[a] Regina de F. P. M. Moreira,[c] J. Arturo Santaballa,[d] Moisés Canle.[d]

[a] *Departamento de Química and [c] Departamento de Engenharia Química e de Alimentos, Universidade Federal de Santa Catarina, 88040-670 Florianópolis, SC, Brazil.*

[b] *Department of Chemistry, University College London, 20 Gordon Street, London*

WC1H OAJ, U.K.

[d] *Universidade da Coruña. Grupo Reactividade Química e Fotorreactividade (React!), Departamento de Química, Facultade de Ciencias & CICA, E-15071 A Coruña, Spain.*

1. On leave from: Instituto Federal de Educação, Ciência e Tecnologia do Rio Grande do Sul, Feliz, RS, Brazil.

ORCID authors

Eduardo Humeres	https://orcid.org/0000-0002-9740-2756
Corresponding author	E-mail: eduardo.humeres@ufsc.br
Abil E. Aliev	https://orcid.org/0000-0001-8725-3550
Alessandra Smaniotto	https://orcid.org/0000-0002-3525-257X
Rafael Brognoli	http://orcid.org/0000-0002-7726-2477
Nito Angelo Debacher	https://orcid.org/0000-0002-8809-8457
Regina de F. P. M. Moreira	https://orcid.org/0000-0002-2863-7260
J. Arturo Santaballa	https://orcid.org/0000-0003-0593-8009
Moisés Canle	https://orcid.org/0000-0002-4814-7795

ABSTRACT. Graphite microparticles were oxidized to graphene oxide (MPGO) by Hummers´ method followed by thermal exfoliation (C/O ratio 1.53). Graphene oxide was modified with SO_2 (mMPGO) at 600 °C and by subsequent treatment at 200 °C having a sulfur content of 10.9 % (C/O ratio 16.94) and manganese content 9.39 µmol·g^{-1}. The XPS spectrum of MPGO showed the presence of carbonyl and epoxide groups. The reactivity of mMPGO toward alkyl thiol and alkyl amine showed the same selectivity as other carbons and suggested that oxidation did not modify deeply the edging structure of graphite. Therefore, the tetradehydrogenated-benzo[α]anthracene (TBA) reactive site model is valid. From XPS and solid-state NMR, amino-thiolysis occurred via cyclisation. Based on the joint analysis of solid-state ^{1}H and ^{13}C NMR spectra of mMPGOs treated with mono- and difuctionalised alkanes, a preferred conformation of the alicyclic moiety of aminothiol over the graphene matrix occurred via binding to mMPGO at both amine and thiol ends. It was found that paramagnetic manganese ions in mMPGO can lead to cross-polarisation inefficiency in the ^{13}C CPMAS detection of alkyl chains bound to mMPGO, while ring currents from graphene aromatic layers can shift alkyl ^{1}H NMR signals to lower frequencies by up to 4 ppm.

INTRODUCTION

Graphite, diamonds, fullerenes are naturally occurring allotropes of carbon. Graphite is one of the main precursors for the synthesis of graphene oxide and reduction of graphene oxide can give graphene like structures.[1,2] The oxidation of graphene may occur by the excitation of the π electrons along with oxide functional groups that share the π electrons to form sp^3 hybridization for graphene oxide material.[3] The widely known Hummers' method of oxidation[4] has been modified and improved in several ways with respect to the conventional techniques.[5] The graphene oxide reduction produces reduced-graphene oxide by numerous chemical, thermal, solvothermal, electrochemical, microwave or photoreduction techniques.[5,6]

Different structural models have been proposed to describe the chemical structure of graphene oxides.[7-13] Nonetheless, there is no consensus about its chemical structure, because the non-stoichiometric character of the synthetic methods. The structural model proposed by Lerf-Klinowski is widely recognized (Fig. 1).[14]
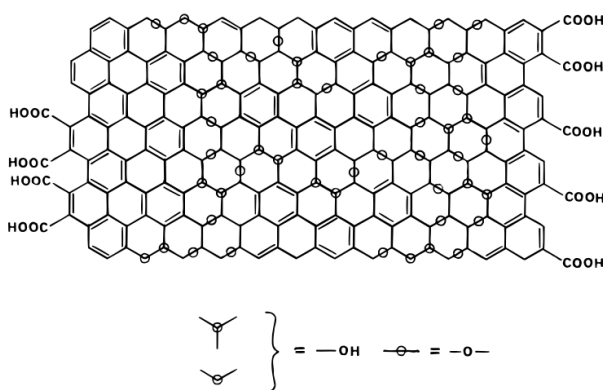

Figure 1. Lerf-Klinowski model for graphene oxide.[12]

This model assumes an uncorrelated random distribution of epoxy and alcohol groups on the surfaces, with alcohol and carboxyl groups around the edges. The oxidized sites on the solid surface are ascribed to the oxidation of carbon double bonds, that are

more reactive than conjugated/aromatic systems. Moreover, the graphene oxide surface of the model also presents two different parts randomly spread: some aromatic regions with unoxidized benzenic rings, and extended conjugated regions, formed by 6-membered alicyclic rings supporting C=C, C-OH and O-C-O groups on the basal plane, in addition to C=O and COOH groups in terminal positions.[11,15] More recently, a structural model similar to the Lerf-Klinowski model has been proposed that include more groups such as lactols, sulfate and peroxysulfate esters.[16-18]

Monolayer graphene exhibits remarkable optical properties, high intrinsic strength, superior thermal conductivity and extremely high charge carrier mobility.[19] Moreover, the propagation of massless electrons through the honeycomb lattice in a sub-micrometer distance without scattering makes it possible to investigate the quantum effects in graphene even at room temperature.[2,19,20] Graphene-based hybrid materials with special optical and conductive properties can be obtained by functionalization with different groups.[21-23] In particular insertion of sulfur into graphite produces superconductive composites[24,25] and can increase the efficiency of fuel cells.[26] Sulfur modification activates carbon particles for further functionalization.[27,28]

Incorporation of sulfur functionalities in carbon matrices can be achieved by reduction of SO_2 on carbons whose mechanism has been extensively studied.[29] Theoretical calculations on the chemisorption of SO_2 on partially dehydrogenated pyrene as model of graphite[30] showed that only physical adsorption can occur on the basal plane while the most favorable site was a triplet biradical zigzag edge that is fully occupied at 900 ºC. A dioxathiolane is formed by the OO approach and is at equilibrium with a γ-sultine formed by the SO approach. Sulfur intermediates were observed during the reduction of SO_2 on a variety of carbons (graphite,[31] graphite oxide,[32] graphene oxide,[32] activated carbon,[33] carbon nanotubes,[34] charcoal[31]). The XPS spectra of the residual

4

carbons after the reaction with SO_2 showed in the S2p region at 168 eV a band assigned to the oxidized sulfur of the dioxathiolane and at 164 eV a second band of non-oxidized sulfur assigned to a *o*-benzyno or thiirene.[35]

A reactive site model was proposed to describe all the steps of the reduction reaction of SO_2 on carbons (Fig. 2).[35] The proposed graphite reactive model was 1,2,11,12-tetradehydrogenated-benzo[α]anthracene (TBA, Fig. 2), where position 11-12 is the zigzag diradical site of the initial chemical absorption of SO_2, and position 1-2 is a benzyne bond that adds the sulfur transferred from the dioxathiolane to form a thiirene. The theoretical calculations on the TBA model of the energetic of the mechanism produced results according to the experimental values. The barrier for the sulfur transfer from the dioxathiolane **1** to the thiirene **3** was calculated as $\Delta G^{\ddagger} = 39.4$, kcal·mol^{-1} for graphite at 900 °C (activated carbon, $\Delta G^{\ddagger}_{exp} = 42.39$ kcal.mol^{-1}, at 630 °C)[35], and the barrier for the decarboxylation reaction from the dioxathiolane **1** was $\Delta G^{\ddagger} = 111$ kcal·mol^{-1} (graphite, $\Delta G^{\ddagger}_{exp} = 107\text{-}114$ kcal·mol^{-1}, at 900 °C)[31].
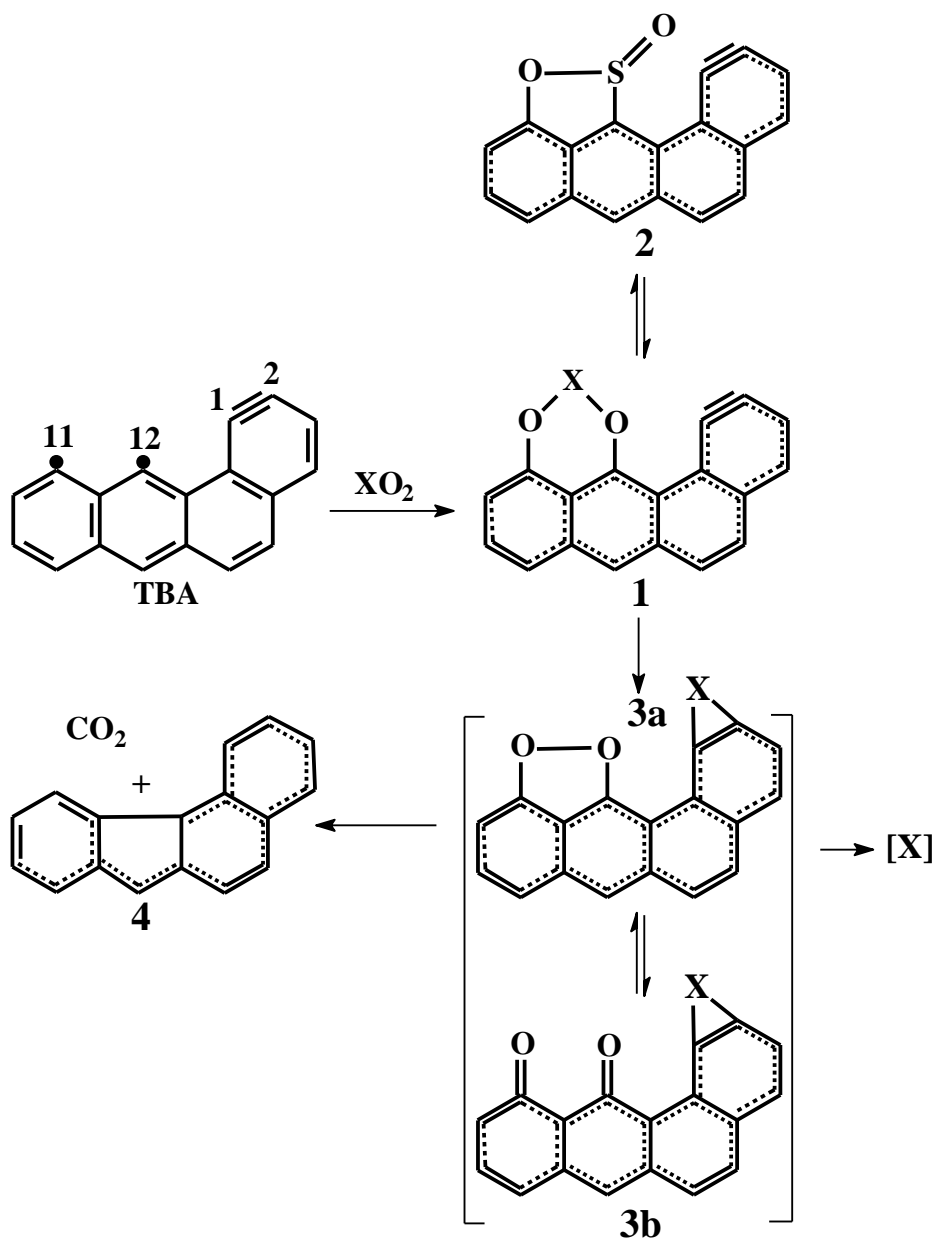
Figure 2. Mechanism of reduction of SO_2 and ozone on carbons (X = S, O). TBA

model.[35,36]

The reactive site model behaves as a molecular reactor that performs all the steps

of the reduction to produce CO_2 and elemental sulfur.[35] The site of insertion of SO_2 in the

carbon matrix is on a diradical in the zigzag edge forming two oxidized sulfur reactive

intermediates (1,3,2-dioxathiolane **1** and 1,2-oxathietane 2-oxide or γ-sultine **2**) in equilibrium.[30] The dioxathiolane transfers the sulfur to a benzyne bond forming a non-oxidized sulfur intermediate thiirene along with [peroxide **3a** ⇌ dicarbonyl **3b**] tautomers that eliminate CO_2 through isomerization of the peroxide tautomer **3a** to an oxirane and subsequent steps.[35]

The TBA model was also used successfully for the mechanism of reduction of ozone on graphite (Fig. 2).[36] Ozone is isoelectronic with sulfur dioxide and both reactions have the same stoichiometry (eq 1)

$$O=O=O + C \rightarrow \tfrac{1}{2} X_2 + CO_2 \qquad (X = S, O) \qquad (1)$$

Insertion of ozone at the diradical site produces a trioxolane that transfers the oxygen forming an oxirene and the same tautomers as SO_2. There was a balance of oxygen between the number of moles of inserted ozone and the moles of the oxygen eliminated from total decarboxylation. Consequently, the activation parameters at 700 °C of the decarboxylation reaction of graphite after SO_2 reduction ($\Delta G^{\ddagger} = 96.1$ kcal·mol^{-1})[31] were the same as the values obtained after ozone reduction ($\Delta G^{\ddagger} = 95.7$ kcal·mol^{-1}).[36]

Sulfur and oxygen transport route out the carbon matrix is initiated from tautomers **3** by extrusion of the element from the thiirene or the oxirene (Fig. 2). The non-oxidized sulfur intermediate is an unstable thiirene. Benzyne adds elemental sulfur to give a benzothiirene and a series of polysulfane compounds.[37-40] The stability of o-benzopolysulfanes o-$C_6H_4S_x$ increases with x from 1 to 2 (disulfane, −39 kcal·mol^{-1}) to 3 (trisulfane, −48 kcal·mol^{-1}).[41]

In the reduction of ozone on graphite, tautomers **3** contain oxygen as an oxirene (Fig. 2) that extrudes atomic oxygen. Benzooxirene is unstable but *ab initio* calculations

indicated that it exists at a minimum as intermediate[42] and is stabilized by benzoannelation.[43]

The mechanism of sulfur transport from the thiirene was postulated after the study of the effect of salts on the reduction of SO_2 on carbons (Fig. 3).[35,44]
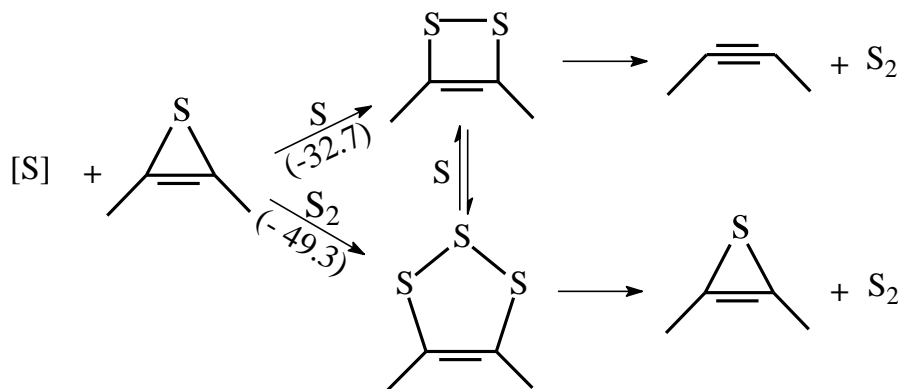

Figure 3. Mechanism of sulfur transport. Values in parenthesis calculated from TBA model, in kcal·mol^{-1}.

The atomic sulfur extruded from the thiirene reacts with another thiirene site to generate a more stable disulfane (-32.7 kcal mol^{-1}) which might eliminate S_2 and regenerate the benzyne site, or accepts another atomic sulfur to form a still more stable trisulfane (-49.3 kcal mol^{-1}) that can extrude S_2 regenerating the thiirene. Trisulfane can also be generated from the thiirene by addition of S_2. The calculated stabilization energies of disulfane and trisulfane are similar to the values mentioned above for the stability of o-benzopolysulfanes.[41]

Atomic oxygen from the oxirene, produced during the ozonation of graphite, is eliminated as molecular oxygen or is intercalated in the graphite matrix (Fig. 4).[36]

Intercalated oxygen can react with new incoming atoms to produce O_2 molecules or can form epoxy groups with adjacent C atoms.
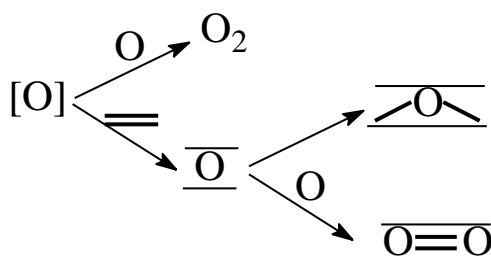

Figure 4. Mechanism of oxygen transport of the reduction of ozone on graphite.[36]

Insertion of the oxidized and non-oxidized sulfur intermediates of the reduction of SO_2 on graphene oxide was obtained by thermal treatment and nonthermal plasma[45] and the relative content of each intermediate could be controlled through thermal interconversion.[46] The intermediates presented selective reactivities toward thiols and amines. Insertion of alkyl thiols occurred only on the oxidized intermediates while alkyl amines reacted only with the non-oxidized intermediate. This behavior has been observed for non-oxidized carbon as graphite, and oxidized carbons as graphite oxide, graphene oxide and activated carbon.[32,46,47] XPS spectra and atom inventory technique,[48] along with solid-state NMR were used to postulate the mechanisms.

The thiolysis mechanism was consistent with the one proposed for 2,5-disubstituted thienosultines.[47,49] Nucleophilic displacement of the alkylthiol on the O-carbon atom of the sultine or the dioxathiolane ring gives a sulfinate or a dioxathiolate with insertion of the alkylthiol and elimination of SO_2 that might reinsert on the diradical site (Fig. 5).[32]
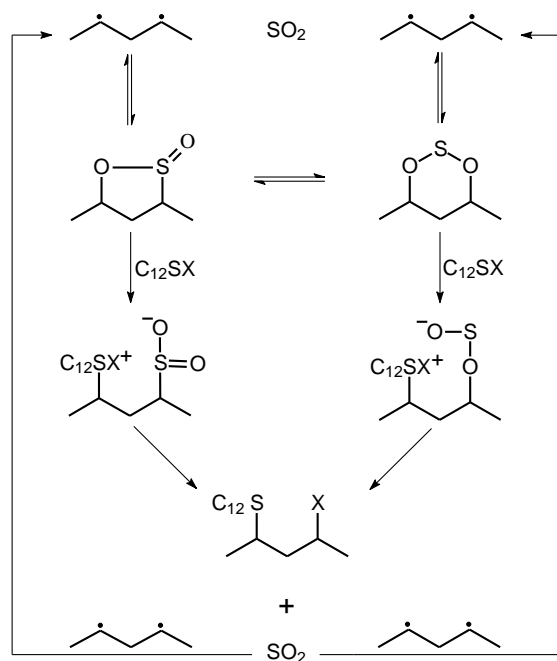
Figure 5. Reactions of the oxidized sulfur intermediate with dodecane-1-thiolate X ($C_{12}X$, X= Na^+, H^+).

The XPS spectrum after the aminolysis showed the insertion of nitrogen at 400 eV of the alkylamine with opening of the thiirene ring and some decarboxylation (Fig. 6).[32]
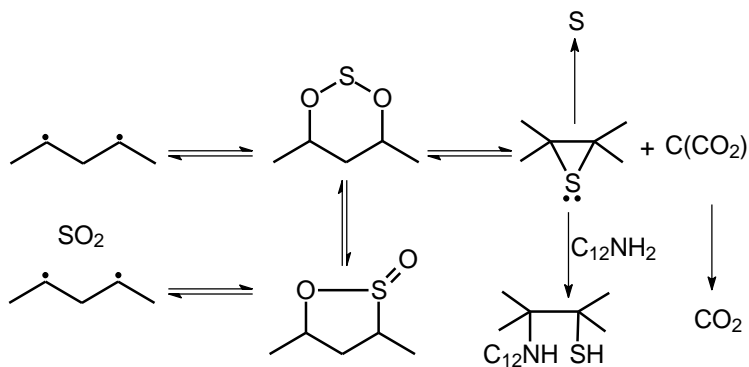

Figure 6. Reaction of the nonoxidized sulfur intermediate with dodecylamine ($C_{12}NH_2$).

The reversibility of the reduction reaction[33] and the easy interconversion of the intermediates, suggested that the dioxathiolane site is near the thiirene site and that an amino-thiolysis should produce a double functionalization with cyclisation in the same reactive site. In this work we present the results addressed to this question. The amino-thiolysis of modified graphene oxide by SO_2 with 11-amino-1-undecanethiol was consistent with the double functionalization according to the XPS calculations, and the cyclisation was shown by the results of the solid-state NMR detailed study.

EXPERIMENTAL SECTION

Graphite microparticles, MPG, from Cia. Nacional de Graphite, Brazil, had a composition of 99.92% carbon, 0.08% ash and 0.02% moisture; the d_{50} value was 6.20 μm. Sulfur dioxide 99.9% was from Veronese & Cia Ltda and Helium 99.9% was supplied by White & Martins, Brazil. The reagents were of analytical purity from Sigma-Aldrich and were used without further purification.

X-Ray photoelectron spectroscopy. The XPS analysis of the samples was performed using a Thermo Scientific K-Alpha ESCA instrument equipped with aluminum Kα monochromatized radiation at 1486.6 eV X-ray source. Due to the no conductor nature of samples it was necessary to use an electron flood gun to minimize surface charging. Neutralization of the surface charge was performed by using both a low energy flood gun (electrons in the range 0 to 14 eV) and a low energy Argon ions gun. Spectra were acquired at 10^{-9} mbar. The XPS measurements were carried out using monochromatic Al-Ka radiation (hν = 1486.6 eV). Photoelectrons were collected from a take-off angle of 90º relative to the sample surface. The measurement was done in a Constant Analyser Energy mode (CAE) with a 100 eV pass energy for survey spectra and 20 eV pass energy for high resolution spectra. Charge referencing was done by setting

the lower binding energy C1s photo peak at 285.0 eV. Surface elemental composition was determined using the standard Scofield photoemission cross sections.

Solid-State ^{13}C NMR Spectroscopy. Solid-state NMR experiments were carried out on Bruker Avance 300 spectrometer with 7.05 T wide-bore magnet at ambient probe temperature. High-resolution solid-state ^{13}C were recorded at 75.5 MHz using a standard Bruker 4 mm double-resonance magic-angle spinning (MAS) probe. Solid materials were packed into zirconia rotors of 4 mm external diameter and spun at MAS frequencies of 8 kHz and 12 kHz with stability better than ±3 Hz. High-resolution solid-state ^{13}C NMR spectra were recorded using cross-polarization (CP), MAS and high-power proton decoupling. Typical acquisition conditions for ^{13}C CPMAS experiments were: ^{1}H 90° pulse duration = 2.7 µs; contact time = 2 ms; recycle delay = 5 s; MAS frequency = 8 kHz. The amplitude ramp on the ^{1}H channel was employed in CPMAS experiments. A 30% ramp was achieved by a linear change of the pulse radiofrequency amplitude from 70% to 100%. From CPMAS optimization on the standard glycine sample, the 30% ramp provided higher signal-to-noise ratio than 50% or 10% ramps. Proton-decoupled ^{13}C MAS spectra were also acquired using the sequence of Cory and Ritchey with the direct detection of ^{13}C nuclei. The following acquisition conditions were used: ^{13}C 90° pulse duration = 5 µs; recycle delay = 30 s; MAS frequency = 12 kHz. Additionally, ^{1}H MAS spectra were recorded using a single-pulse excitation with a 2.4 µs long pulse (recycle delay = 5 s; MAS frequency = 12 kHz). The ^{13}C and ^{1}H chemical shifts are given relative to tetramethylsilane (TMS). The ^{13}C chemical shifts were calibrated using glycine (176.46 ppm). A liquid sample of DMSO-d_6 was used for ^{1}H chemical shift referencing. The chemical shift of the residual ^{1}H signal due to DMSO-d_5 was assigned to 2.49 ppm.

Graphene oxide. Graphene oxide was obtained from graphite microparticles by the Hummers' method modified by Bissessur.[4,50] Sulfuric acid, 95%, 230 mL, was transferred

to a cylindrical glass reactor cooled to 0 °C and graphite microparticles (MPG), 10 g, were added with mechanical stirring. Then, 30 g of $KMnO_4$ were slowly added maintaining agitation and keeping the temperature from exceeding 20 °C. The mixture was cooled to 2 °C and stirred without refrigeration for 30 min, allowing to warm up to room temperature. Distilled water, 230 mL, was slowly added to the reactor avoiding excessive heating. The mixture was transferred to a 5 L beaker and 1.4 L of water was added with stirring followed by 100 mL of 30% hydrogen peroxide. The particles were exhaustively washed by centrifugation, decanting the supernatant and adding distilled water, until no precipitation of $BaSO_4$ upon addition of $BaCl_2$ solution. Graphene oxide (MPGO) was dried at 100 °C for four days and the particles were exfoliated at 300 °C for 15 minutes (C/O ratio 1.53).[51] FTIR spectrum: 3400 cm^{-1} (broad, OH); 1710 cm^{-1} (COOH); 1640, 1576 cm^{-1} (C=C, carbon rings); 1110, 1038 cm^{-1} (C-O-C).[52-57]

Modification of graphene oxide MPGO with SO_2 (mMPGO).[46] The sample was placed in the middle of a tubular quartz reactor and heated by an electric oven for *ca*. 30 min to reach 600 °C under a flow of Ar (40 mL·min^{-1}). The flow was then changed to pure SO_2 (50 mL min^{-1}) for 6 h (sulfur content 12.0%). This sample was submitted to a subsequent treatment at 200 °C with pure SO_2 at 50 mL min^{-1} for 2 h, producing mMPGO containing 10.9% S and C/O ratio 16.94.

Measurement of manganese content. Manganese content in mMPGO (9.92 mg) was determined by graphite furnace atomic absorption spectroscopy (GFAAS). Operating temperatures were 1000 °C for ashing and 2400 °C for atomizing; Pd/Mg was used as modifier for thermal stability. Manganese concentration was 9.39 µmol/g.

Reactivity of graphene oxide modified with SO_2. mMPGO, 100 mg, was allowed to react with 100 mg of the reagent (dodecane-1-amine, dodecane-1-thiol, or 11-amino-1-

undecanethiol), refluxing in dried DMSO for 48 h. The solid was filtered and intensively washed with dried ethanol and dried under vacuum (100 mmHg, 56 °C) for 6 h.

RESULTS AND DISCUSSION

Oxidation of graphite to graphene oxide. Graphene oxide has a layered structure whose degree of oxidation depends on the synthetic method.[51,58] Therefore, a detailed chemical structure cannot be resolved because of the pseudo-random chemical functionalization of each layer. Several structural models for graphite oxide have been proposed [7-12] and recent structural models suggest that in graphene oxides the two-dimensional planar structure of graphite might be significantly deviated.[13,59] However, these structural models are centered on the chemical functionalization and do not describe appropriately the relationship between the reactivity and geometry of the carbon matrix. To this end the model must contain the relevant groups that determine its reactivity and the products, and their relative positions.

Hummers´ oxidation of graphite[4] proceeds first by intercalation of sulfuric acid increasing the interlayer distance.[60,61] The oxidation agents are permanganic acid and the ozone formed *in situ*. Although ozone formation has been observed during the reaction of potassium permanganate in H_2SO_4 solutions, its presence depends on the acid concentration. Hummers´ oxidation occurs in 18 M (96%, specific density 1.84 $g \cdot cm^{-3}$) sulfuric acid, where Mn(VII) decomposes unimolecularly upon heating (80-100 °C) to oxidize water and yield molecular oxygen (E_a = 28 $kcal \cdot mol^{-1}$).[62] O_3 is not formed under these conditions. It could not be found under Hummers´ oxidation conditions[18] but was observed in the UV-Vis spectra after addition of water in the concentrated H_2SO_4 solution of $KMnO_4$.[63] The rate of formation of ozone increases with the activity of water and reaches a maximum at 12 M sulfuric acid (E_a = 17 $kcal \cdot mol^{-1}$, below 50 °C), in a parallel

route with the oxidation of water to oxygen, and decomposes almost completely to oxygen.[62]

If we assume that the oxidation was only due to ozone, the XPS spectrum of graphene oxide (MPGO) showed the expected insertion of ozone, with oxygen as carbonyl and epoxide groups, except for a small concentration of hydroxilates (7.90 at%) that might be due to permanganic acid oxidation (Table 1). The permanganic acid oxidative mechanism might produce atomic oxygen that intercalates in the interlayer channels and by consecutive reactions generate epoxide groups by a mechanism similar to ozone. Calculation of the spectrum by the atom inventory technique,[48] showed that 43.6% of the mass of MPGO (100 g) would be due to inserted ozone. As was mentioned above, oxidation of graphite by ozone produced [peroxide⇌dicarbonyl] tautomers, that eliminate CO_2 (Fig. 2), and atomic oxygen that intercalates in the graphite (Fig. 4).[36] Atomic oxygen would produce mainly epoxide groups by basal oxidation.

The present results suggest that the oxidation of graphite to graphene oxide occurred mainly at the edges and then extended to the internal basal planes. Therefore, the basal oxidation would produce epoxide groups with no essential damage of the carbon network because the ozone reduction reactive sites are located at the edges of the carbon matrix and the TBA reactive site model should be valid.

Table 1. XPS spectrum of graphite MPG and after oxidation to MPGO[a]

Sample	Initial MPG		MPGO[b]		
Element	eV (weight%)	at%	eV (weight%)	at%	Calc at%[c]
C1s					
C=C	285.0 (100)	94.91	285.0 (59.25)	35.84	
C-O			286.08(26.29)	15.91	
C=O			288.14(14.46)	8.75	
total		94.91		60.50	60.50
O1s	533.0 (100)	5.09			
C=O			532.46(35.16)	13.89	
C-O-C			534.28 (44.83)	17.71	
Na-O			535.75 (20.01)	7.90	
total		5.09		39.50	39.50
C/O		18.65		1.53	

[a] Spectrum calibrated by reference to C1s (285.0 eV). [b] Oxidation according by Hummers'
method modified by Bissessur.[50] [c] Calculated from reaction $C + O_3 \rightarrow C(O_3)$

Graphene oxide after thermal modification with SO_2. Thermal modification of
graphene oxide MPGO with SO_2 was first carried out at 600 °C followed by subsequent
heating at 200 °C. The XPS spectrum shown in Table 2 was calculated from Fig. 2 (X=S)
by reactions (1), (2), and (3).

$$3 \xrightarrow{600\,°C} 4 + CO_2 \tag{1}$$

$$TBA + SO_2 \rightarrow 1 \rightarrow 3 \tag{2}$$

$$3 \xrightarrow{200\,°C} 4 + CO_2 \tag{3}$$

Table 2. Binding energies and composition from XPS spectrum of graphene oxide (MPGO) and after SO_2 modification (mMPGO).[a]

Sample	MPGO[b]		mMPGO [c]		Calc.[d]
Element	eV (weight%)	at%	eV (weight%)	at%	
S2p non-oxi			164.0 (94.3)	1.61	
oxi			167.4 (5.7)	0.10	
total				1.71	1.86
C1s C=C	285.0 (59.25)	35.84	285.0 (91.8)	85.20	
C-O	286.08(26.29)	15.91	286.2 (6.09)	5.65	
C=O	288.14(14.46)	8.75	287.3 (2.11)	1.96	
total		60.50		92.81	92.81
O1s C=O	532.46(35.16)	13.89	531.1 (19.0)	1.04	
C-O-C	534.28 (44.83)	17.71	533.4 (81.0)	4.44	
Na-O	535.75 (20.01)	7.90			
total		39.50		5.48	5.33
C/O		1.53		16.94	17.41

[a] Spectrum calibrated by reference to C1s (285.0 eV). [b] Oxidation by Hummers' method modified by Bissessur.[4,50] The particles were exfoliated at 300 ºC for 15 minutes (C/O ratio 1.53). [c] Flow of SO_2 100 mL·min^{-1}; at 600 ºC for 6 h and subsequent heating at 200 ºC for 2 h. [d] Calculated from reactions (1), (2), (3).

Reaction (1) shows that the main elimination of CO_2 occurred at 600 ºC and 58.7% of the initial mass of graphene oxide was eliminated as CO_2 (Table 3) while the proper modification reaction of SO_2 insertion is reaction (2), with some decarboxylation at 200 ºC (Reaction (3).

Table 3. Weight composition (%) of MPGO after heating step at 600 $^{\circ}$C during modification with SO_2.[a]

Element	n_i[b]	f=0.457 Δ	CO₂ At-moles $n_i\Delta$	CO₂ Weight, g $(AW)n_i\Delta$[c]	MPGO At% Initial $C_{i\ exp}$	MPGO Weight Initial, g $(AW)C_i\ exp$[b]	MPGO Weight% final	MPGO At% total $C_{f\ final}$
S2p								
C1s	-1	18.11	-18.11	-217.32	60.50	726.00	508.68	92.82
O1s	-2		-36.22	-579.52	39.50	632.00	52.48	7.18
Σn_i	-3							
Total			-54.33	-796.84[b]	100.00	1358.00	561.16	100.00
Weight %				CO₂ (58.7%)		100%	MPGO (41.3%)	

[a] Calculated according to reaction (1). [b] CO_2. [c] AW, atomic weight.

Reactivity of graphene oxide modified with SO₂ (mMPGO). Monoatomic sulfur extruded from the thiirene initiates a series of consecutive reactions shown in Fig. 3, between reactive sites to insert in the thiirene ring and subsequent sulfanes. The reactive site can to be visualized as part of an ensemble of sites where the model represents the statistically predominant structure present when the steady-state is reached.[35] Most members of the ensemble have a free energy very close to the mean value. In other words, the reactive sites of the systems under the steady state are very similar and contribute to the total free energy with about the same value. Therefore, it is possible to represent this ensemble by one reactive site model. When the steady state is reached under the flow of a constant gas atmosphere, there will be a constant concentration of reactive site species $(TBA)_j$ related to the reactions occurring in the systems.

The observed reaction of graphene oxide modified by SO$_2$ with alkyl thiol and alkyl amine shown in Table 4 indicates that the TBA model can be used and the spectra were calculated by the atom inventory method.[48] As was mentioned above, both reactions followed the same selectivity observed for other carbons with respect to the intermediates. The calculated spectra agreed very closely with the experimental elemental content.

Table 4. Binding energies and composition from XPS spectrum of MPGO thermally modified with SO$_2$ after thiolysis, aminolysis and amino-thiolysis reactions.[a]

Sample	mMPGO[b]		After thiolysis[c]		Calc[d]	After aminolysis[e]		Calc[f]	After amino-thiolysis[g]		Calc[h]
Element	eV (weight%)	at%	eV (weight%)	at%	at%	eV (weight%)	at%	at%	eV(weight %)	at%	at%
S2p non-oxi	164.0 (94.3)	1.61	164.3 (90.9)	5.12		164.4 (87.2)	3.64		164.2 (88.4)	3.55	
oxi	167.4 (5.7)	0.10	166.9 (9.2)	0.52		166.5 (12.8)	0.54		166.5 (11.6)	0.47	
total		1.71		5.64	5.38		4.18	3.95		4.02	4.58
C1s	285.0 (91.8)	85.20	285.0 (78.8)	70.54		285.0 (68.9)	61.47		285.0 (69.1)	59.12	
						285.7 (5.8)	5.16		285.8 (6.3)	5.35	
	286.2 (6.09)	5.65	286.2 (15.4)	13.76		286.2 (18.8)	16.75		286.3 (17.2)	14.76	
	287.3 (2.11)	1.96	287.7 (5.8)	5.18		287.3 (6.5)	5.82		287.7 (7.5)	6.39	
total		92.81		89.48	89.74		89.24	90.19		85.62	85.82
O1s									530.9 (8.4)	0.78	
	531.1 (19.0)	1.04	531.2 (32.1)	1.57		532.2 (57.7)	3.23		532.6 (34.4)	3.17	
	533.4 (81.0)	4.44	533.7 (67.9)	3.31		533.9 (42.3)	2.36		534.1 (52.1)	4.78	
									535.9 (5.1)	0.47	
total		5.48		4.88	4.88		5.59	4.88		9.19	8.44
N1s		-		-		400.7	0.98	0.98	400.5	1.17	1.17
C/O		16.94		20.00			16.67			0.90	

[a]Spectrum calibrated by reference to C1s (285.0 eV). [b]Flow of SO$_2$ 100 mL·min^{-1}; at 600 °C for 6 h and subsequent heating at 200 °C for 2 h. [c]Reflux with dodecane-1-thiol (C$_{12}$SH) in DMSO for 48 h. [d]From reactions (4), (5). [e]Reflux with dodecylamine (C$_{12}$NH$_2$) in DMSO for 48 h. [f] From reactions (6), (7), (8). [g]Reflux with 11-amino-undecanethiol (HSC$_{11}$NH$_2$) in DMSO for 48 h. [h]From reactions (9), (10).

In Fig. 7, species **1** e **2** (from Fig. 2) are expected to react with extruded elemental sulfur generating species **5** and **6**. The composition after thiolysis with dodecane-1-thiol ($C_{12}SH$), increased in sulfur content, is shown in Table 4 calculated from the reactions (4) and (5), corresponding to the insertion of the thiol and partial decarboxylation.
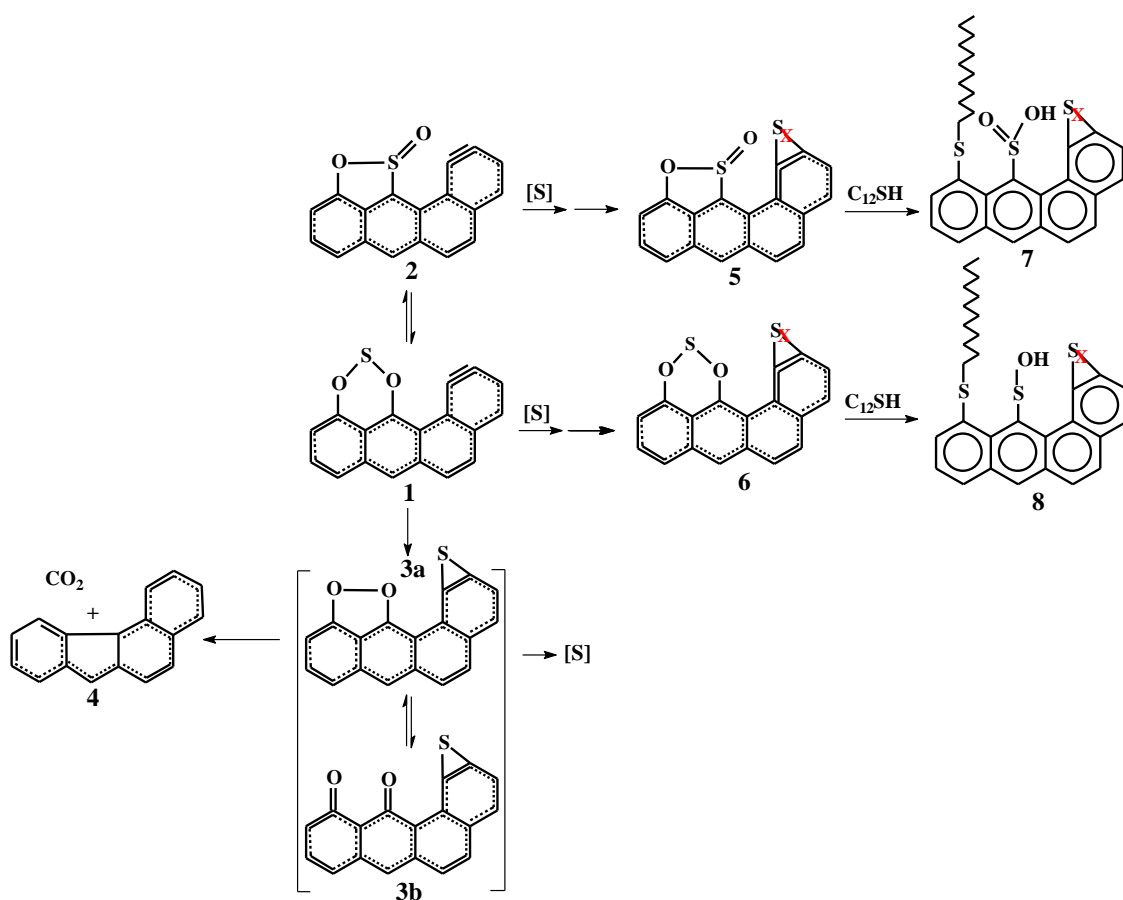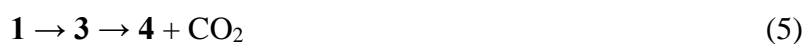
$$\mathbf{5} \text{ (or } \mathbf{6}) + C_{12}SH \rightarrow \mathbf{7} \text{ (or } \mathbf{8}) \tag{4}$$

$$\mathbf{1} \rightarrow \mathbf{3} \rightarrow \mathbf{4} + CO_2 \tag{5}$$

Figure 7. Thiolysis of modified graphene oxide with dodecane-1-thiol ($C_{12}SH$), X = 1-3. TBA model.

The aminolysis with dodecane-1-amine can be described by Fig. 8, where species **5** and **6** were generated through the same reactions as the thiolysis of Fig. 7.
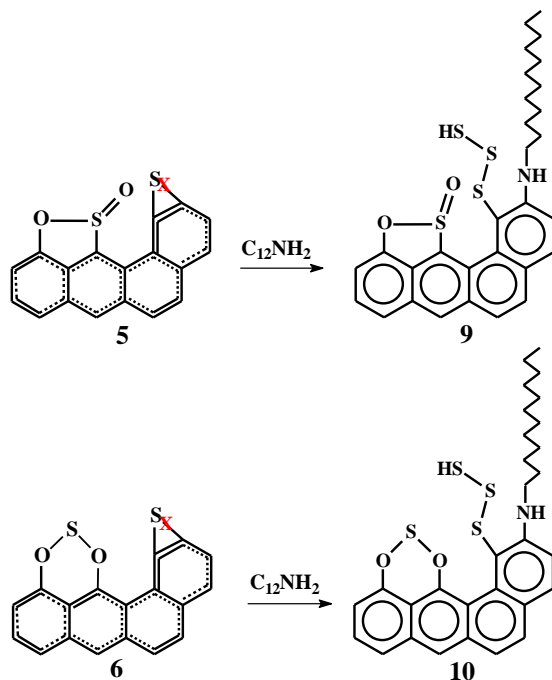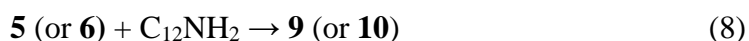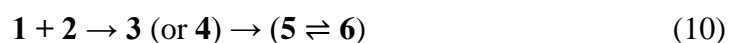

Figure 8. Aminolysis of modified graphene oxide with dodecane-1-amine ($C_{12}NH_2$), $X = 3$. TBA model.

The XPS showed the insertion of nitrogen and the composition was calculated by equations (6), (7) with insertion of SO_2 and partial decarboxylation, and equation (8) with insertion of the amine.

$$TBA + SO_2 \rightarrow \mathbf{1} \tag{6}$$

$$\mathbf{1} \rightarrow \mathbf{3} \rightarrow \mathbf{4} + CO_2 \tag{7}$$

$$\mathbf{5} \text{ (or } \mathbf{6}) + C_{12}NH_2 \rightarrow \mathbf{9} \text{ (or } \mathbf{10}) \tag{8}$$

It was considered that the nonoxidized sulfur intermediate in the modified graphene oxide at the steady state should be as trisulfane that is the most stable form.[35,41] Thiirene and cyclosulfanes react with amines as the thiiranes, with S_N2 ring opening.[64-66]

Amino-thiolysis of graphene oxide modified with SO$_2$. The amino-thiolysis of mMPGO after reaction with 11-amino-undecanethiol showed a XPS with an increased content of sulfur and nitrogen. The calculated spectrum in Table 4 considered the cyclisation mechanism of the amino-thiolysis as described in Fig. 9. Reaction (9) describes the modified TBA reacting with SO$_2$ to generate **1**, as in Fig. 7, considering only the OO approach of SO$_2$. The initial TBA species **1** is assumed to have the steady state composition with the dioxathiolane oxidized intermediate at position 11,12 and the reduced intermediate at position 1,2 in the form of the more stable trisulfane. Reaction (10) is the amino-thiolysis, as thiolysis **3** or aminolysis **4,** followed by the cyclisation reaction (**5** ⇌ **6**).

$$\text{TBA} + \text{SO}_2 \rightarrow \mathbf{1} \tag{9}$$

$$\mathbf{1} + \mathbf{2} \rightarrow \mathbf{3} \text{ (or } \mathbf{4}) \rightarrow (\mathbf{5} \rightleftharpoons \mathbf{6}) \tag{10}$$

Reaction on the dioxathiolane opens the ring inserting the thiol on position 11 or 12 while reaction on the trisulfane opens the ring inserting the amino group on position **1** or **2**. There is no apparent selectivity on those positions and in Fig. 9 were chosen arbitrarily positions 11 and 2 because there would be less steric constrain for the cyclisation in the next step.
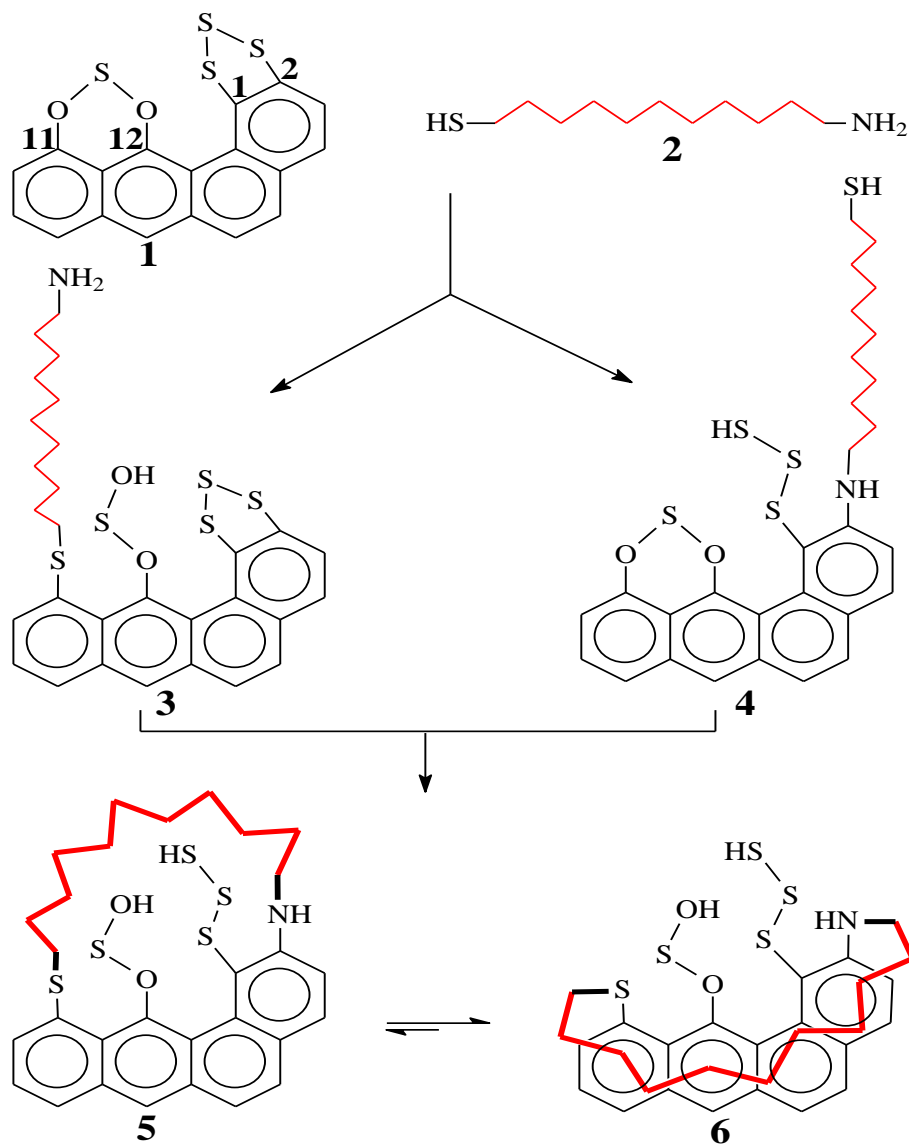
Figure 9. Amino-thiolysis cyclisation mechanism of graphene oxide modified with SO$_2$. TBA model.

The cycle formed as the result of amino-thiolysis can have two main conformations. The outer conformation **5** is external to TBA site while the inside conformation **6** is bent over the graphene matrix.

The bent-over cyclic conformation should present a preferred minimum energy conformation over the graphenic matrix due to the positive interactions between the alkyl moiety and the graphene layer. Noncovalent interactions are widespread in organic

systems and can play a decisive role in their properties. Interactions between sp^3-C-H bonds and aryl substituents have been observed,[41] also supported by quantum chemical calculations.[64-66] The activity of Hoveyda-Grubbs 2nd generation catalyst was reduced when bound to carbonaceous filler (graphite, graphene or carbon nanotubes) because the strong π-stacking interaction with the aryl groups.[68] Metal nanoparticle catalysts supported on 2D nanomaterials, as graphene oxide, are able to induce different interactions (Van der Waals, π-π stacking, dipole-dipole) varying the functional groups on the ligands (alkyl, aromatic).[69] Solid polymer electrolytes intercalate into graphite oxide due to the dipole–dipole and/or hydrogen bonding forces of attraction between the polymers and graphene oxide.[50] A computational study on the interaction between pristine graphene and graphene oxide and several polymers found that the lowest energy conformer of the β-conformation of polyvinylidene fluoride with the hydrogen atoms facing the graphene had the strongest interaction.[70]

The XPS data in Table 4 shows that the cyclisation has occurred because although species **3** and **4** have the same composition as cyclized species **5 ⇌ 6**, the simultaneous insertion of **2** accounts for the concentration of S and N in species **5 ⇌ 6** without increasing the concentration of carbon. This subject will be also discussed using the NMR results.

Solid-state NMR studies. Modified graphene oxides after aminolysis with dodecane-1-amine (**1**), thiolysis with dodecane-1-thiol (**2**) and amino-thiolysis with 11-amino-undecanethiol (**3**) were studied using solid-state ^{1}H and ^{13}C MAS NMR measurements. Since the solid materials were exhaustively washed and then dried under vacuum, we expected the remaining solids to be free of small molecular weight organic molecules adsorbed on the surface or of those included as free molecules in the bulk of the material, unless bonded covalently to the solid particles.

The ^{13}C MAS spectra acquired with a direct observation of ^{13}C nuclei using the sequence of Cory and Ritchey[74] (Fig. 10), and decoupling from protons, showed only a single broad signal for each sample centered at approximately 124 ± 3 ppm with the linewidth of ~3 kHz (**1**), ~2 kHz (**2**) and ~4 kHz (**3**). Unlike the spectrum of graphene oxide,[16] no signals were observed at 60-70 ppm in ^{13}C MAS spectra of (**1**)-(**3**). This was expected, as the C/O ratio increased from 1.53 in MPGO to 16.94 in mMPGO (see above). The ^{13}C MAS spectra of mMPGO shown in Fig. 10 were similar to the ^{13}C MAS spectra of reduced graphene oxide (RGO),[75] although the reported chemical shift for RGO is 117 ppm. Previously, broad ^{13}C signals at 134,[76] 130,[11,12] 129,[16] 128[77] and 117 ppm[75] have been assigned to sp^2 carbons of aromatic rings and conjugated double bonds in graphite oxides and graphene oxides. It is likely that the variation over a wide range of 17 ppm is caused by the changes in relative contents of aromatic and olefinic carbons, as well as by the relative content of sp^2 carbons attached to oxygen atoms.
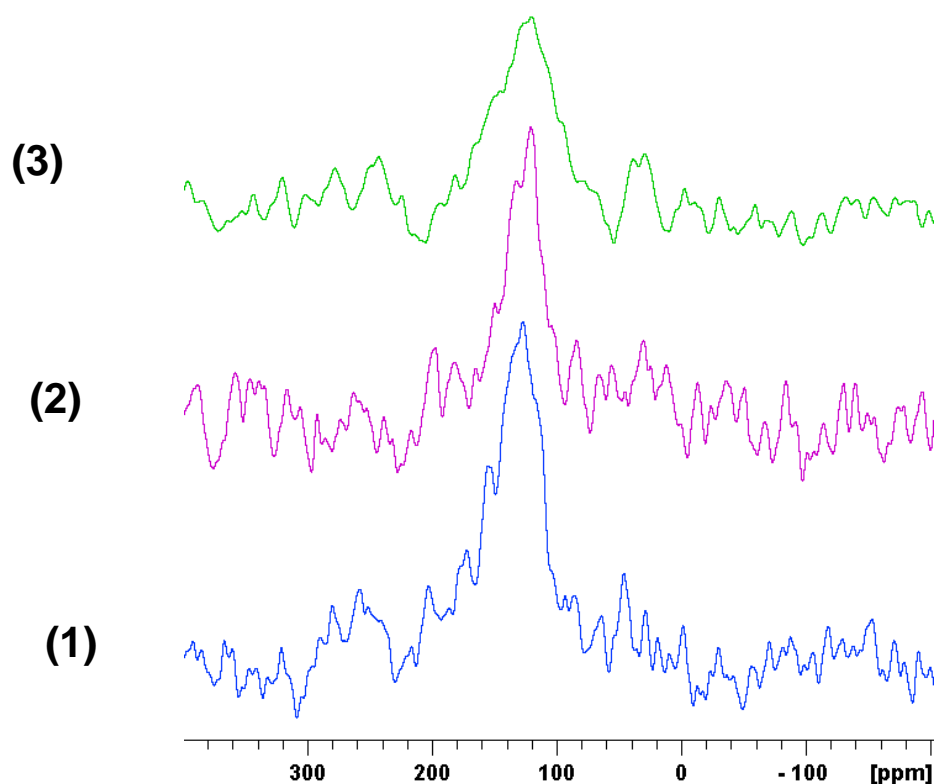
Figure 10. Proton-decoupled ^{13}C MAS spectra of (**1**), blue; (**2**), red; (**3**), green, acquired using the sequence of Cory and Ritchey with direct detection of ^{13}C nuclei.[74]

In addition to the signal at ~125 ppm, another broad signal at approximately 29 ppm was observed with a linewidth of ~1.2 kHz in the ^{13}C CPMAS spectra of **1** and **2** (Fig. 11), which have been attributed to aliphatic carbons.[32,47] Thus, while the sensitivity of the experiment with direct observation of ^{13}C nuclei was not sufficient for the detection of aliphatic carbons, it was possible to enhance the signal due to protonated carbons of a dodecyl chain in the experiment which utilises cross-polarisation from ^{1}H nuclei to ^{13}C nuclei. In particular, the carbons of the $(CH_2)_9$ of a $-CH_2-(CH_2)_9CH_2CH_3$ group resonate at ~29 ppm, while the remaining methylene and methyl carbons of the dodecyl group are not resolved due to the very broad line observed.[32,47] Unlike **1** and **2**, no signal was

observed in the ^{13}C CPMAS spectrum of **3**. <mark>In the first instance,</mark> this suggests that the content of organic species with C-H bonds <mark>may be</mark> negligibly small in **3**, hence cross-polarisation from protons is inefficient for revealing any carbons in the vicinity of ^{1}H nuclei. However, XPS of the aminolysis and thiolysis reaction of modified MPGO under the same conditions, did show the insertion of the alkyl moiety as well as the insertion of the amino-thiol (Table 4). <mark>The solid-state ^{1}H MAS spectra discussed below are also in favor of the insertion of the alkyl moiety in all three samples studied.</mark>
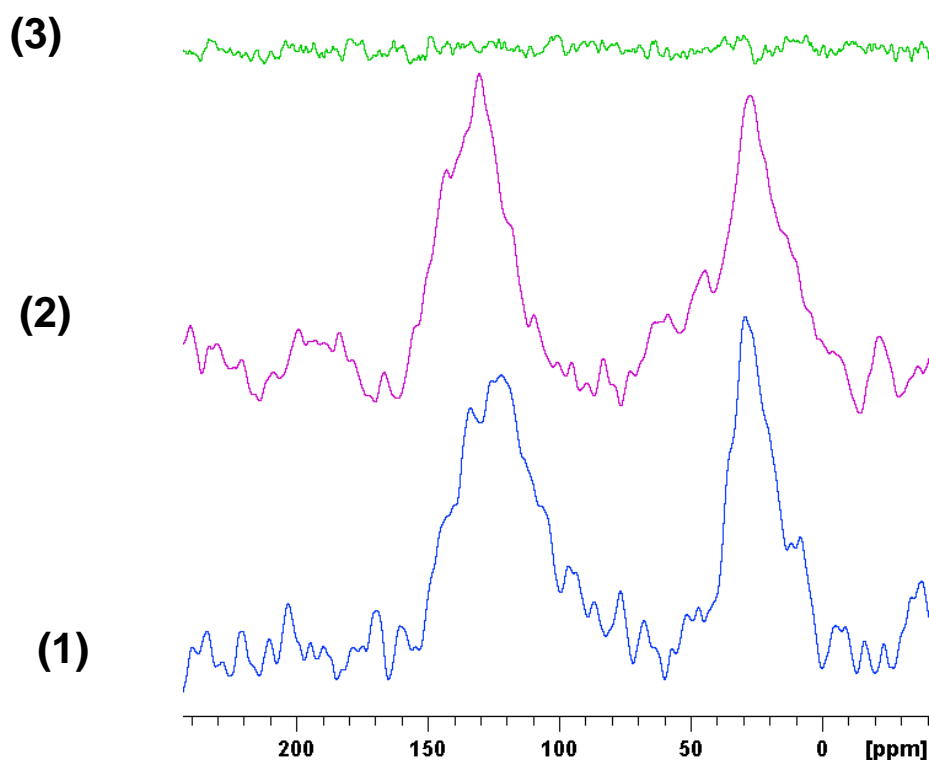
Figure 11. ^{13}C CPMAS spectra of (**1**) – (**3**).

The ^{1}H MAS spectra (Fig. 12) showed isotropic signals at <mark>-1.5 ± 0.3 ppm (**1**), -1.6 ± 0.3 ppm (**2**) and -2.8 ± 0.3 ppm (**3**). The measured linewidths were 2.6 ± 0.2 KHz (**1**), 2.4 ± 0.2 KHz (**2**) and 2.3 ± 0.2 KHz (**3**). Chemical shifts and linewidths were determined from the deconvolution of the isotropic part of the spectrum using two components (see</mark>

Supporting Information). The values quoted above are for the major components in each sample, accounting for >90% of the total integral intensity.
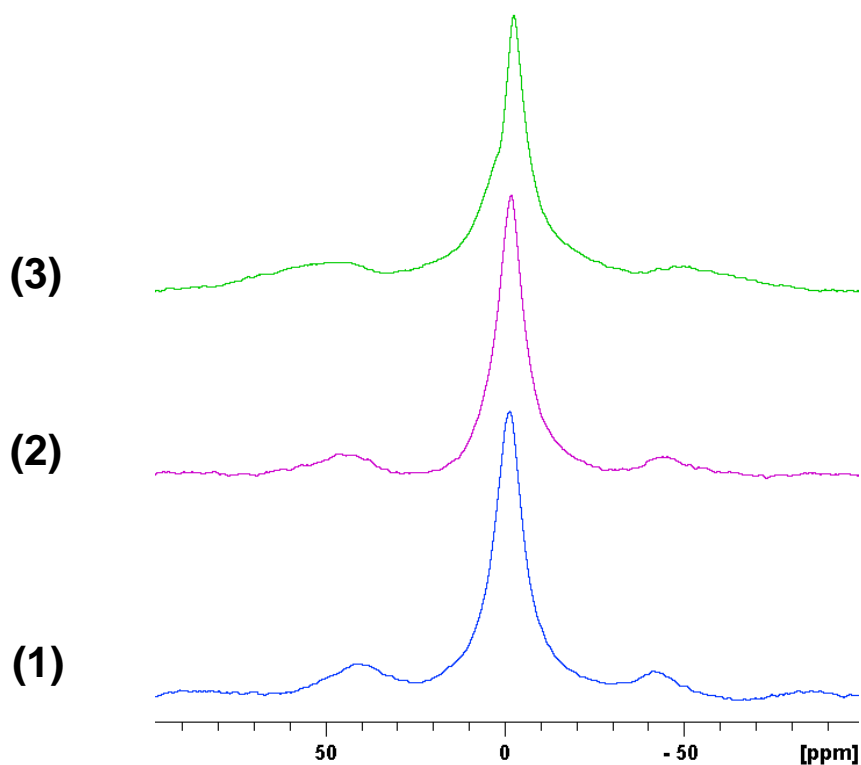

Figure 12. [1]H MAS spectra of (**1**) – (**3**).

We now discuss the ^{1}H and ^{13}C NMR results for mMPGOs (**1**)-(**3**) treated with mono- and difuctionalised alkanes. Compared to ^{13}C, proton chemical shifts show stronger dependence to the changes in the environment and therefore the low frequency negative ^{1}H NMR chemical shifts are likely to be indicative of strong interactions at relatively small distances.[78] As discussed above (see Fig. 9), the di-functionalised alkyl $-S-C_{11}H_{22}-NH-$ is bound to mMPGO at both the sulfur and nitrogen ends of the chain, which is expected to lead to more restricted motional mobility of the $C_{11}H_{22}$ fragment, compared to $C_{12}H_{25}$ chains of mono-functionalised alkyls $C_{12}H_{25}-NH-$ and $C_{12}H_{25}-S-$ bound to mMPGO at only one end of the chain via either sulfur or nitrogen containing

functionalities. The alkyl tails of $C_{12}H_{25}-NH-$ and $C_{12}H_{25}-S-$ can be aligned either perpendicular or parallel to the mMPGO surface. For the perpendicular alignment, protons of the alkyl chain are placed away from the aromatic surface and the expected chemical shift would be near +1.3 ppm for the CH_2 protons, as in normal or functionalised alkanes in solution NMR spectra. The observed chemical shifts in ^1H MAS NMR spectra were -1.5 ppm in (**1**) and -1.6 ppm in (**2**). The ~3 ppm shift to lower frequencies relative to alkanes can be attributed to either the ring current effect from the aromatic rings of the mMPGO surface or to the presence of paramagnetic Mn^{2+} ions. As shown previously, however, the absence of orbital angular momentum in Mn^{2+} leads to an isotropic electron g tensor.[79,80] Thus, nuclear spins such as ^1H or ^{13}C are not expected to experience a pseudocontact shift in the vicinity of Mn^{2+} ions, while they will still experience a paramagnetic relaxation enhancement leading to fast T_1 and $T_{1\rho}$ relaxation of nearby spins. The absence of detectable pseudocontact shifts and paramagnetic residual dipolar couplings for some metal ions, such as Mn^{2+} and Gd^{3+}, has also been attributed to their very low paramagnetic susceptibility anisotropy.[81,82] On the other hand, Fermi contact isotropic shifts due to Mn^{2+} can be very large, if present, of the order of several hundreds of ppm (e. g., estimated as 763 ppm for a ^{31}P nuclei interacting with a Mn^{2+} ion).[83] An aromatic ring current effect is induced under the influence of the external magnetic field and it is observed for ^1H nuclei placed in the vicinity of aromatic rings.[78] It is a widely used phenomenon since the 1950s,[78,84,85] which has also inspired the nucleus dependent chemical shift (NICS) calculations.[86,87] The effect is anisotropic: protons in the molecular plane and outside of the aromatic ring resonate at higher frequencies, while those above or below the ring resonate at lower frequencies.[78] In our case, the parallel alignment of the alkyl chain above the aromatic rings of mMPGO would lead to low-frequency shifts due to the ring current effect. Thus, both the magnitude and the direction of chemical shift

changes in ^{1}H MAS spectra of (**1**)-(**3**) are typical for the ring current effect.[78] For (**3**), the observed chemical shift is -2.8 ppm, i.e. further shift to lower frequencies is observed relative to mono-substituted alkyls (**1**) and (**2**). Compared to free alkanes, the ^{1}H resonance in (**3**) is shifted by -4.1 ppm. The observed large change in the ^{1}H chemical shift value agrees with the structural model in which the disubstituted alkyl in (**3**) is bound to the mMPGO surface at both NH and S ends of the chain, which: (i) restricts the mobility of the the $C_{11}H_{22}$ chain and (ii) places protons of the alkyl chain in closer proximity of the aromatic rings of mMPGO compared to monosubstituted alkyls (**1**) and (**2**). Both the restriction of mobility and shorter distances to the aromatic rings are expected to decrease chemical shift values due to the ring current effect. Thus, the relative changes in ^{1}H NMR chemical shifts agree with the structural model in which the $C_{11}H_{22}$ fragment in (**3**) is bent over the graphene matrix (see conformation **6** in Fig. 9).

Regarding the intramolecular motional mobility and the role of non-covalent C–H…π interactions, although important in rigid cyclic structures, the C-H…π interactions between the C-H bonds of alkyl chains and the aromatic rings of the mMPGO surface are not sufficiently strong to restrict full rotations about the alkyl C–C bonds within the $C_{12}H_{25}$ chain at ambient temperatures, e.g. methyl group rotation or ethyl group rotation about the C_β-C_γ bond of the alkyl chain. Such full rotations cannot take place in the di-functionalised –S–$C_{11}H_{22}$–NH– fragment with both ends of the chain anchored to the mMPGO surface with the di-substituted alkyl chain aligned parallel to the mMPGO surface, as illustrated in Fig. 13. Nevertheless, some restricted dynamics is expected for the cyclic structure, such as interconversion of the ring with the largest motional amplitude at the central carbon atom C_6 of the $(CH_2)_{11}$ chain (Fig. 13).
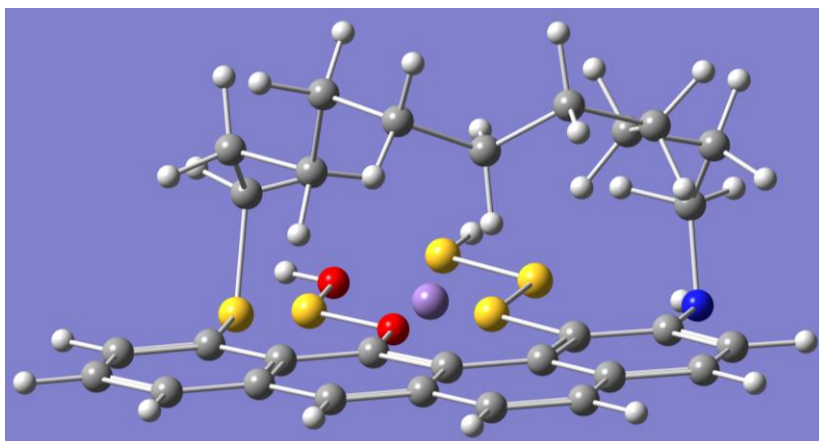
Figure 13. The TBA model after amino-thiolysis cyclisation of 11-amino-1-undecanethiol in the presence of Mn^{2+} ions, illustrating the preferred bent-over conformation of the alkyl chain (Fig. 9). The shown location of Mn^{2+} ion is hypothetical and is used for illustrative purposes only. Atom colors used: gray (carbon); white (hydrogen); red (oxygen); yellow (sulfur); blue (nitrogen); purple (manganese). [88]

The presence of isolated Mn^{2+} ions in graphene oxide and in reduced graphene oxide was previously revealed by Panich *et al.*[89,90] It was attributed to potassium permanganate ($KMnO_4$) used in the oxidation of the sample by Hummers' method. As shown by NMR and EPR measurements,[89,90] these ions are likely to be anchored to the graphene oxide planes and contribute to the ^1H and ^{13}C spin-lattice relaxation. In particular, they showed that the T_1 relaxation time for sp^2 carbons was 110 s in pure polycrystalline graphite and 1.9 s in graphene with manganese ions. As concluded by Panich *et al.*,[90] the only reason for the observed T_1 reduction is the interaction of ^{13}C spins with electron spins of paramagnetic Mn^{2+} ions and that Mn^{2+} ions do not exist as a separate phase but form manganese–graphene charge-transfer complexes and they are positioned on the graphene surface. Note that the concentration of manganese in graphene oxide studied by Panich *et al.* was 3.04 µmol/g, which is significantly less than in

mMPGOs studied in this work (9.39 µmol/g). Similar to conclusions by Panich *et al.*, manganese ions in mMPGOs (**1**)-(**3**) are expected to trigger fast $T_{1\rho}$ relaxation of ^1H spins in spin-locking experiments, which will adversely affect the CP efficiency in ^{13}C CPMAS spectra, since ^{13}C spins cannot cross-polarize from ^1H spins relaxing very fast during the spin-locking period of the CP experiment. The paramagnetic relaxation rate enhancement effects have been shown to depend on the inverse of the 6th power of the metal to the observed nucleus distance (r),[81] thus they are expected to decrease rapidly on a relatively small increase in r. In the case of (**3**) with both ends of alkyl chain anchored to the mMPGO surface, the restricted motional mobility and closer proximity of the $-(CH_2)_{11}-$ chain to the mMPGO surface with manganese ions will result in faster ^1H and ^{13}C spin relaxations compared to (**1**) and (**2**) with mono-substituted $CH_3(CH_2)_{11}-$ chains, thus explaining the complete loss of the CPMAS signal for (**3**) (Fig. 12).

We note that the effect of paramagnetic species on both cross-polarisation and Bloch decay experiments has been subject of the detailed studies previously.[91] Two mechanisms via which paramagnetic species cause signal loss were considered: field inhomogeneity and the interaction between electronic and nuclear spins. Both of these were shown to be efficient in the case of Mn^{2+} ions, which have relatively long spin-lattice relaxation time of the free electron (T_{1e}). Compared to Bloch decay experiments, CP experiments were more susceptible to the interaction between electronic and nuclear spins, which was in turn more efficient for ions with longer T_{1e}, such as Mn^{2+}. The higher susceptibility of CP experiments was attributed to the faster ^1H relaxation during the contact time ($T_{1\rho}$ relaxation): fast relaxation of a ^1H spin close to paramagnetic ions triggers fast relaxation of neighboring ^1H spins via spin diffusion, promoting the signal loss in ^{13}C CPMAS spectra. The degree of signal loss was also higher at higher concentrations of paramagnetic ions. These findings agree well with our analysis of the

CONCLUSIONS

Graphite microparticles, oxidized to graphene oxide (MPGO) by Hummers' method and modified with SO_2, contain manganese. The oxidation can be ascribed mainly to ozone formed during the reaction. Oxygen was inserted as a peroxide⇌dicarbonyl tautomer that was eliminated as CO_2 during the modification at 600 ^{o}C, along with the basal oxidation that produced mainly epoxide groups.

Oxidation did not modify deeply the edging structure of graphite that presented the same selectivity toward thiolysis and aminolysis as nonoxidized carbons. Therefore, the TBA (tetradehydrogenatebenzo[α]anthracene) reactive site model was valid to postulate the mechanisms of these reactions for the graphene oxide modified by SO_2 (mMPGO).

The amino-thiolysis of mMPGO occurred with cyclisation, where the CH_2 groups of the alicyclic moiety of the aminothiol ring adopts a preferred conformation over the graphene matrix. The insertion of the aminothiol occurred in a reactive site, the geometry of which was consistent with the postulated TBA model.

As shown in this work, graphene oxide properties can be modified by functionalization and it is important to optimize the reactivity and selectivity of the reacting centers. The TBA reactive site model works as a molecular reactor that present two reactive sites (diradical and benzyne) that might be chemically or photolytically

functionalized. Both centers become selective when functionalized with the intermediates of the SO$_2$ reduction on a variety of carbons. The selectivity of the two modified centers allowed the insertion of two different functionalities in the same reactive center. Since the functionalization of graphene oxide changes its physical-chemistry properties it can be explored for electronic and biological purposes.

From the point of view of structural characterizations of modified graphene oxides, which are extremely difficult to study by conventional techniques, a chemical variation of the alkyl chain in (**1**), (**2**) and (**3**) with dodecane-1-amine, dodecane-1-thiol and 11-amino-1-undecanethiol, respectively, allowed us to follow the interaction of mono- and disubstituted alkanes with graphene oxide in a sequential manner providing greater insight into the structural changes. In particular, the joint comparative analysis of ^{1}H and ^{13}C solid-state NMR spectra together with the XPS results for different mono- and difuctionalised alkyls allowed us to draw conclusions, which otherwise would be impossible to reach. The changes of ^{1}H NMR chemical shifts of alkyl chains proved particularly useful, which were attributed to ring currents from modified graphene oxides. The efficiency of the ^{1}H-^{13}C cross-polarisation in CPMAS experiments was shown to be driven by the presence of manganese ions in graphene oxides, which provided additional information about the comparative strength and proximity of the interaction between alkyl chains and graphene oxides.

Supporting Information. Additional information on the deconvolution of the isotropic part of the ^{1}H MAS NMR spectra. This material is available free of charge via the Internet at http://pubs.acs.org.

ACKNOWLEDGEMENTS

REFERENCES

1. Sharma, N.; Tomar, S.; Shkir, M.; Choubey, R. K.; Singh, A. Study of Optical Properties of Graphene Oxide. *Mater. Today: Proceedings*, **2021**. 36, 730-735.

2. Yang, G.; Li, L.; Lee, W. B.; Cheung Ng, M. Structure of Graphene and its Disorders: a Review. *Sci. Technol. Adv. Mater.* **2018,** *19*, 613–648.

3. Eda, G.; Lin, Y-Y.; Mattevi, C.; Yamaguchi, H.; Chen, H-A.; Chen, I-C.; Chen, C-W.; Chhowalla, M. Blue Photoluminescence from Chemically Derived Graphene Oxide. *Adv. Mater*. **2010**, *22*, 505-509.

4. Hummers, W. S.; Offeman, R. E. Preparation of Graphitic Oxide. *J. Am. Chem. Soc*. **1958**, *80*, 1339-1339.

5. Ikram, R.; Jan, B. M.; Ahmad, W. An Overview of Industrial Scalable Production of Graphene Oxide and Analytical Approaches for Synthesis and Characterization. *J. Mater. Res. Technol*. **2020**, *9*, 11587-11610.

6. Hussain, A.; Mehdi, S. M.; Abbas, N.; Hussain, M.; Naqvi, R. A. Synthesis of Graphene from Solid Carbon Sources: A focused review, *Mater. Chem. Phys.* **2020**, *248*, 122924.

7. Hofmann, U.; Holst, R. Über die Säurenatur und die Methylierung von Graphitoxyd. *Ber. Dtsch. Chem. Ges. B.* **1939**, *72*, 754-771.

8. Ruess, G. Graphitic Oxide. *Monatsch Chem.* **1946**, *76*, 381-417.

9. Scholz, W.; Boehm, H. P. Untersuchungen am Graphitoxid. VI. Betrachtungen zur Struktur des Graphitoxids. *Z. Anorg. Allg. Chem.* **1969**, *369*, 327-340.

10. Nakajima, T.; Matsuo, Y. Formation Process and Structure of Graphite Oxide. *Carbon,* **1994**, *32*, 469-475.

11. Lerf, A.; He, H.; Riedl, T.; Forster, M.; Klinowski, J. ^{13}C and ^{1}H MAS NMR Studies of Graphite Oxide and its Chemically Modified Derivatives. *Solid State Ion.* **1997**, *101-103*, 857–862.

12. Lerf, A.; He, H.; Forster, M.; Klinowski, J. Structure of Graphite Oxide Revisited. *J. Phys. Chem. B.* **1998**, *102*, 4477–4482.

13. Szabó, T.; Berkesi, O.; Péter F.; Josepovits, K.; Sanakis, Y.; Petridis, D.; Dékány. I. Evolution of Surface Functional Groups in a Series of Progressively Oxidized Graphite Oxides. *Chem. Mater.* **2006**, *18*, 2740–2749.

14. Sinclair, R. C.; Coveney, P. V. Modeling Nanostructure in Graphene Oxide: Inhomogeneity and the Percolation Threshold, *J. Chem. Inf. Model.* **2019**, *59*, 2741–2745.

15. He, H.; Klinowski, J.; Forster, M.; Lerf, A. A New Structural Model for Graphite Oxide. *Chem. Phys. Letters* **1998**, *287*, 53-56.

16. Cai, W.; Piner, R. D.; Stadermann, F. J.; Park, S.; Shaibat, M. A.; Ishii, Y.; Yang, D.; Velamakanni, A.; An, S. J.; Stoller, M.; An, J.; Chen, D.; Ruoff, R. S.

Synthesis and Solid-State NMR Structural Characterization of ^{13}C-Labeled Graphite Oxide, *Science* **2008**, *321*, 1815-1817.

17. Gao, W.; Alemany, L. B.; Ci, L.; Ajayan, P. M. New Insights Into the Structure and Reduction of Graphite Oxide, *Nat. Chem.* **2009**, *1*, 403-408.

18. Groveman, S.; Peng, J.; Itin, B.; Diallo, I.; Pratt, L. M.; Greer, A.; Biddinger, E. J.; Greenbaum, S. G.; Drain, C. M.; Francesconi, L.; Vittadello. M. The Role of Ozone in the Formation and Structural Evolution of Graphene Oxide Obtained from Nanographite, *Carbon* **2017**, *122*, 411-421.

19. Geim, A. K. Graphene: Status and Prospects. *Science* **2009**, *324*, 1530–1534.

20. Denis, P. A.; Iribarne, F. Comparative Study of Defect Reactivity in Graphene, *J. Phys. Chem. C*, **2013**, *117*, 19048–19055.

21. Ansari, S.; Giannelis, E. P. Functionalized Graphene Sheet-Poly(vinylidene fluoride) Conductive Nanocomposites. *J. Polym. Sci. Part B: Pol. Phys.* **2009**, *47*, 888-897.

22. Liu, Z. B.; Xu, Y. F.; Zhang, X. Y.; Zhang, X. L.; Chen, Y. S.; Tian, J. G. Porphyrin and Fullerene Covalently Functionalized Graphene Hybrid Materials with Large Nonlinear Optical Properties. *J. Phys. Chem. B*. **2009**, *113*, 9681–9686.

23. Geng, J.; Jung, H. T. Porphyrin Functionalized Graphene Sheets in Aqueous Suspensions: From the Preparation of Graphene Sheets to Highly Conductive Graphene Films. *J. Phys. Chem. C*. **2010**, *114*, 8227–8234.

24. Kurmaev, E. Z.; Galakhov, A. V.; Moewes, A.; Moehlecke, S.; Kopelevich, Y. Interlayer conduction band states in graphite-sulfur composites. *Phys. Rev. B*. **2002**, *66*, 193402-193405.

25. Silva, R. R.; Torres, J. H. S.; Kopelevich, Y. Indication of Superconductivity at 35 K in Graphite-Sulfur Composites. *Phys. Rev. Lett.* **2001**, *87*, 147001-147005.

26. Coen, M. C.; Keller, B.; Groening, P.; Schlapbach, L. Functionalization of graphite, glassy carbon, and polymer surfaces with highly oxidized sulfur species by plasma treatments. *J. Appl. Phys.* **2002**, *92*, 5077-5083.

27. Love, J. C.; Estroff, L. A.; Kriebel, J. K.; Nuzzo, R. G.; Whitesides, G. M. Self-Assembled Monolayers of Thiolates on Metals as a Form of Nanotechnology. *Chem. Rev.* **2005**, *105*, 1103−1169.

28. Derda, R.; Wherritt, D. J.; Kiessling, L. L. Solid-Phase Synthesis of Alkanethiols for the Preparation of Self-Assembled Monolayers. *Langmuir* **2007**, *23*, 11164–11167.

29. Humeres, E.; Debacher, N. A.; Moreira, R. F. P. M.; Santaballa, J. A.; Canle, M. Mechanisms of Solid-gas Reactions: Reduction of Air Pollutants on Carbons, *Top. Catal.* **2020**, *63*, 817-832.

30. Pliego, J. R.; Resende. S. M.; Humeres, E. Chemisorption of SO_2 on Graphite Surface: A Theoretical Ab Initio and Ideal Lattice Gas Model Study. *Chem. Phys.* **2005**, *314*, 127–133.

31. Humeres, E.; Moreira, R. F. P. M.; Peruch, M. G. B. Reduction of SO_2 on Different Carbons. *Carbon* **2002**, *40*, 751–760.

32. Humeres, E.; Castro, K. M.; Smaniotto, A.; Lopes, C. N.; Debacher, N. A.; Moreira, R. F. P. M.; Schreiner, W. H.; Aliev, A. E. Reactivity of the Intermediates of the Reduction of SO_2. Functionalization of Graphite, Graphite Oxide and Graphene Oxide. *J. Phys. Org. Chem.* **2014**, *27*, 344–351.

33. Humeres, E.; Peruch, M. G. B.; Moreira, R. F. P. M.; Schreiner, W. H. Reactive Intermediates of the Reduction of SO_2 on Activated Carbon. *J. Phys. Org. Chem.* **2003**, *16*, 824–830.

34. Humeres, E.; Souza, E. P; Debacher, N. A.; Moreira, R. F. P. M.; Lopes, C. L.; Pérez, M. I. F.; Santaballa, J. A.; Canle, M.; Schreiner, W. H.; Aliev, A. E. *Langmuir* **2015**, *31*, 164–170.

35. Humeres, E.; Debacher, N. A.; Moreira, R. F. P. M.; Santaballa, J. A.; Canle, M. Reactive Site Model of the Reduction of SO_2 on Graphite. *J. Phys. Chem. C*, **2017**, *121*, 14649-14657.

36. Humeres, E.; Castro, K. M.; Debacher, N. A.; Moreira, R. F. P. M. Reaction Mechanism of the Reduction of Ozone on Graphite. *Langmuir* **2020**, *36*, 11225–11236.

37. Nakayama, J.; Kashiwagi, M.; Yomoda, R.; Hoshino, M. Reactions of elemental sulfur and selenium with dimethyl acetylenedicarboxylate, methyl propiolate and benzyne. *Nippon Kagaku Kaishi*, **1987**, *7*,1424-1429.

38. Nakayama, J.; Akimoto, K. Reactions of benzyne with sulfur compounds. *Sulfur Reports*, **1994**, *16*, 61-111.

39. Font, J.; Torres, M.; Gunning, E.; Strausz, O. P. Gas-Phase Photolysis of 1,2,3-Thiadiazoles: Evidence for Thiirene Intermediates. *J. Org. Chem*. **1978**, *43*, 2487-2490.

40. Torres, M.; Clement, A.; Bertie, J. E.; Gunning, E.; Strausz, O. P. Low-Temperature Matrix Isolation of Thiirenes. *J. Org. Chem*. **1978**, *43*, 2490-2493.

41. Brzostowska, E. M.; Greer, A. Polysulfane Antitumor Agents from o-Benzyne. An Odd-Even Alternation Found in the Stability of Products o-$C_6H_4S_x$ (x = 1-8). *J. Org. Chem.* **2004**, *69,* 5483-5485.

42. Lewars, E. Benzooxirene. Ab Initio Calculations. *J. Mol. Struct. (Theochem)*. **1996**, *360*, 67-80.

43. Lewars, E. Benzooxirene, Naphthooxirenes, and Anthraceneoxirenes: the Stabilization of the Oxirene System by Bond Fixation in Acenes. A comparison of Ab Initio and DFT in the Investigation of Annelated Oxirenes. *Can. J. Chem.* **2000**, *78*, 297–306.

44. Humeres, E.; Peruch, M. G. B.; Moreira, R. F. P. M.; Schreiner, W. H. Reduction of Sulfur Dioxide on Carbons Catalyzed by Salts. *Int. J. Mol. Sci.* **2005**, *6*, 130–142.

45. Humeres, E.; Debacher, N. A.; Smaniotto, A.; Castro, K. M.; Benetoli, L. O. B.; Souza, E. P.; Moreira, R. P. F. M.; Lopes, C. N.; Schreiner, W. H.; Canle, M.; Santaballa, J. A. Selective Insertion of the Sulfur Dioxide Reduction Intermediates on Graphene Oxide. *Langmuir* **2014**, *30*, 4301–4309.

46. Smaniotto, A.; Humeres, E.; Debacher, N. A.; Castro, K. M.; Benetoli, L. O. B.; Schreiner, W. H.; Canle, M.; Santaballa, J. A. Interconversion and Selective Reactivity of Sulfur Dioxide Reduction Intermediates Inserted on Graphene Oxide. *J. Phys. Org. Chem.* **2016**, *29*, 773–780.

47. Humeres, E.; Castro, K. M.; Moreira, R. F. P. M.; Peruch, M. G. B.; Schreiner, W. H.; Aliev, A. E.; Canle, M.; Santaballa, J. A.; Fernandez, I. Reactivity of the Thermally Stable Intermediates of the Reduction of SO_2 on Carbons and Mechanisms of Insertion of Organic Moieties in the Carbon Matrix. *J. Phys. Chem. C* **2008,** *112*, 581–589.

48. Humeres, E.; Castro, K. M.; Moreira, R. F. P. M.; Schreiner, W. H.; Aliev, A. E.; Canle, M.; Santaballa, J. A.; Fernandez, I. The Use of XPS Spectra for the Study

of Reaction Mechanisms: The Atom Inventory Method. *J. Phys. Org. Chem.* **2008**, *21*, 1035–1042.

49. Liu, W.-D.; Chi, C.-C.; Pai, I.-F.; Wu, A.-T.; Chung W.-S. Synthesis of 2,5-Disubstituted Thienosultines and Their Thermal Reactions with Dienophiles and Nucleophiles. *J. Org. Chem.* **2002**, *67*, 9267-9275.

50. Bissessur, R.; Scully, S. F. Intercalation of Solid Polymer Electrolytes Into Graphite Oxide. *Solid State Ion.* **2007**, *178*, 877-882.

51. Talyzin, A. V.; Szabo, T.; Dekany, I.; Langenhorst, F.; Sokolov, P. S.; Solozhenko, V. L. Nanocarbons by High-Temperature Decomposition of Graphite Oxide at Various Pressures. *J. Phys. Chem. C* **2009**, *113,* 11279–11284.

52. Paredes, J. I.; Villar-Rodil, S.; Martínez-Alonso, A.; Tascón, J. M. D. Graphene Oxide Dispersions in Organic Solvents. *Langmuir* **2008,** *24,* 10560-10564.

53. Hontoria-Lucas, C.; López-Peinado, A. J.; López-González, J. D.; Rojas-Cervantes, M. L.; Martín-Aranda, R. M. Study of oxygen-containing groups in a series of graphite oxides: Physical and chemical characterization. *Carbon* **1995**, *33*, 1585-1592.

54. Xu, Y.; Bai, H.; Lu, G.; Li, C.; Shi, G. *J.* Flexible Graphene Films via the Filtration of Water-Soluble Noncovalent Functionalized Graphene Sheets. *Am. Chem. Soc.* **2008**, *130*, 5856–5857.

55. Stankovich, S.; Piner, R. D.; Nguyen, S. T.; Ruoff, R. S. Synthesis and exfoliation of isocyanate-treated graphene oxide nanoplatelets. *Carbon* **2006**, *44*, 3342–3347.

56. Bourlinos, A. B.; Gournis, D.; Petridis, D.; Szabó, T.; Szeri, A.; Dékány, I. Graphite Oxide: Chemical Reduction to Graphite and Surface Modification with Primary Aliphatic Amines and Amino Acids. *Langmuir* **2003**, *19*, 6050–6055.

57. Fuente, E.; Menéndez, J. A.; Díez, M. A.; Suárez, D.; Montes-Móran, M. A. Infrared Spectroscopy of Carbon Materials: A Quantum Chemical Study of Model Compounds. *J. Phys. Chem. B* **2003**, *107*, 6350-6359.

58. You, S.; Luzan, S. M.; Szabó, T.; Talyzin, A. V. Effect of Synthesis Method on Solvation and Exfoliation of Graphite Oxide. *Carbon* **2013**, *52*, 171-180.

59. Boukhvalov, D. W.; Katsnelson, M. I. Modeling of graphite oxide. *J. Am. Chem. Soc*. **2008**, *130*, 10697-10701.

60. Dimiev, A. M.; Tour, J. M. Mechanism of Graphene Oxide Formation. *ACS Nano* **2014**, *8*, 3060−3068.

61. Krishnamoorthy, K.; Veerapandian, M.; Yun, K.; Kim, S.-J. The Chemical and Structural Analysis of Graphene Oxide with Different Degrees of Oxidation. *Carbon* **2013**, *53*, 38−49.

62. Dzhabiev, T. S.; Denisov, N. N.; Moiseev, D. N.; Shilov, A. E. Formation of Ozone During the Reduction of Potassium Permanganate in Sulfuric Acid Solutions. *Russ. J. Phys. Chem. (Zhurnal Fizicheskoi Khimii*) **2005**, *79*, 1755−1760.

63. Chen, J.; Zhang, Y.; Zhang, M.; Yao, B.; Li, Y.; Huang, L.; Li, C.; Shi, G. Water-Enhanced Oxidation of Graphite to Graphene Oxide with Controlled Species of Oxygenated Groups. *Chem. Sci*. **2016**, *7*, 1874–1881.

64. Turk, S. D.; Louthan, R. P.; Cobb, R. L.; Bresson, C. R. Direction of ring opening in the reaction of episulfides with amines. *J. Org. Chem*. **1964**, *29*, 974-975.

65. Kakiuchi, H.; Iijima, T.; Horie, H. The ring-opening reactions of propylene oxide and propylene sulfide with dibutylamine. *Tetrahedron* **1979**, *35*, 303-308.

66. Banks, H. D.; White, W. E. A computational study of the reactions of thiiranes with ammonia and amines. *J. Org. Chem*. **2001**, *66*, 5981-5986.

67. Cheng, S.-Y.; Qu, Y.-X.; Tao, Z.; Zhou, K.-Z.; Wei, L.-T.; Wang, C.; Zhao, W.-W.; Jiang, D.-F.; Ma, P.-H. The Host-Guest Properties Observed Between the Viologens and Cyclopentanocucurbit[6]uril. *Austral. J. Chem*. **2020**, *73*, 601-607.

68. Murayama, H.; Heike, Y.; Higashida, K.; Shimizu, Y.; Yodsin, N.; Wongnongwa, Y.; Jungsuttiwong, S.; Mori, S.; Sawamura, M. Iridium-Catalyzed Enantioselective Transfer Hydrogenation of Ketones Controlled by Alcohol Hydrogen-Bonding and sp^3-C-H Noncovalent Interactions. *Adv. Syn. & Cat.* **2020**, *362*, 4655-4661.

69. Sajjad, M. A.; Harrison, J. A.; Nielson, A. J.; Schwerdtfeger, P. Interplay of Steric and Electronic Effects on the Bonding Components in Aromatic Ring Agostic Interactions. *Organometallics* **2017**, *36*, 4231-4237.

70. Wheeler, S. E.; Seguin, T. J.; Guan, Y.; Doney, A. C. Noncovalent Interactions in Organocatalysis and the Prospect of Computational Catalyst Design. *Acc. Chem. Res*. **2016**, *49*, 1061-1069.

71. Mariconda, A.; Agovino, A.; Sirignano, M.; Guadagno, L. Strong Interaction with Carbon Filler of Polymers Obtained by Pyrene Functionalized Hoveyda-Grubbs 2nd Generation Catalyst. *Polymers* **2019**, *11*, 1261(1-12).

72. Low, S. S.; Gang, S.; Shon, Y.-S. Interaction of Ligand-capped Metal Nanoparticles with 2D Atomic Layered Nanomaterials. Abstracts of Papers, 249th ACS National Meeting & Exposition, Denver, CO, USA, March 22-26, **2015**.

73. Guryel, S.; Alonso, M.; Hajgato, B.; Dauphin, Y.; Van Lier, G.; Geerlings, P.; De Proft, F. A Computational Study on the Role of Noncovalent Interactions in the Stability of Polymer/graphene Nanocomposites. *J. Mol. Mod*. **2017**, *23*, 1-14.

74. Cory, D. G.; Ritchey, W. M. Suppression of Signals from the Probe in Bloch Decay Spectra. *J. Magn. Reson.* **1988**, *80*, 128-132.

75. Das, T. K.; Banerjee, S.; Pandey, M.; Vishwanadh, B.; Kshirsagar, R. J.; Sudarsan. V. Effect of Surface Functional Groups on Hydrogen Adsorption Properties of Pd Dispersed Reduced Graphene Oxide. *Int. J. Hydrogen. Energ.* **2017**, *42*, 8032-8041.

76. Hontoria-Lucas, C.; López-Peinado, A. J.; López-González, J. de D.; Rojas-Cervantes, M. L.; Martín-Aranda, R. M. Study of oxygen-containing groups in a series of graphite oxides: Physical and chemical characterization, *Carbon* 1995, *33 (11)*, 1585-1592.

77. Vacchi, I. A.; Spinato, C.; Raya, J.; Bianco, A; Ménard-Moyon, C. Chemical reactivity of graphene oxide towards amines elucidated by solid-state NMR. *Nanoscale* **2016**, *8*, 13714-13721.

78. Gunther, H. NMR Spectroscopy: Basic Principles, Concepts and Applications in Chemistry. Chichester; New York: Wiley **1994**. 2nd ed.; 581 pages.

79. Farkas, D.; Hansson, Ö. An NMR study elucidating the binding of Mg(II) and Mn(II) to spinach plastocyanin. Regulation of the binding of plastocyanin to subunit PsaF of photosystem I, *Biochim. Biophys. Acta* **2012**, *1807*, 1539-1548.

80. Clore, G.M.; Iwahara, J. Theory, practice, and applications of paramagnetic relaxation enhancement for the characterization of transient low-population states of biological macromolecules and their complexes, *Chem. Rev.* **2009**, *109*. 4108-4139.

81. Bertini, I.; Luchinat, C.; Parigi, G.; Pierattelli, R. NMR Spectroscopy of Paramagnetic Metalloproteins. *ChemBioChem* **2005**, *6*, 1536-1549.

82. Parigi, G.; Luchinat, C. NMR Consequences of the Nucleus–Electron Spin Interactions. In *Paramagnetism in Experimental Biomolecular NMR*; Luchinat,

C., Parigi, G., Ravera, E., Eds; New Developments in NMR No. 16; Royal Society of Chemistry, 2018, pp. 1-41.

83. Pell, A. J.; Pintacuda, G. Broadband solid-state MAS NMR of paramagnetic systems. *Prog. Nucl. Magn. Reson. Spectrosc.* **2015**, *84-85*, 33-72.

84. Pople, J. A. Molecular orbital theory of aromatic ring currents, *Mol. Phys.* **1958**, *1*, 175–180.

85. McWeeny, R. Ring currents and proton magnetic resonance in aromatic molecules. *Mol. Phys.* **1958**, *1*, 311-321.

86. Schleyer, P. v. R.; Maerker, C.; Dransfeld, A.; Jiao, H.; Hommes, N. J. R. v. E. Nucleus-Independent Chemical Shifts: A Simple and Efficient Aromaticity Probe. *J. Am. Chem. Soc.*, **1996**, *118*, 6317-6318.

87. Báez-Grez, R.; Ruiz, L.; Pino-Rios, R.; Tiznado, W. Which NICS method is most consistent with ring current analysis? Assessment in simple monocycles. *RSC Adv.* **2018**, *8*, 13446-13453.

88. GaussView, Version 6.1, Roy Dennington, Todd A. Keith, and John M. Millam, Semichem Inc., Shawnee Mission, KS **2016**.

89. Panich, A. M.; Shames, A. I.; Sergeev, N. A. Paramagnetic Impurities in Graphene Oxide. *Appl. Magn. Reson.* **2013**, *44*, 107-116.

90. Panich, A.M.; Shames, A.I.; Aleksenskii, A.E.; Dideikin, A. Magnetic Resonance Evidence of Manganese-graphene Complexes in Reduced Graphene Oxide, *Solid State Commun.* **2012**, *152*, 466-468.

91. Smernik, R. J.; Oades, J. M. Paramagnetic Effects on Solid State Carbon-13 Nuclear Magnetic Resonance Spectra of Soil Organic Matter. *J. Environ. Qual.* **2002**, *31 (2)*, 414-420.

Table of Contents Graphic

Intramolecular Amino-thiolysis Cyclisation of Graphene Oxide Modified with Sulfur Dioxide: XPS and Solid-state NMR Studies.

Eduardo Humeres, Abil E. Aliev, Alessandra Smaniotto, Rafael Brognoli,

Nito A. Debacher, Regina de F. P. M. Moreira, J. Arturo Santaballa, Moisés Canle.